Egypt. J. Chem. **Vol. 68**, No. 5 pp. 179 - 192 (2025)

Egyptian Journal of Chemistry

http://ejchem.journals.ekb.eg/

Synthesis and characterization of functionalized cerium and zirconium metal- organic frameworks as novel solid acid catalysts for hydrogen generation

Ahmed Abdo Hassan*, Mostafa Farrag, R. M. Gabr

Chemistry Department, Faculty of Science, Assiut University, Assiut, Egypt

Abstract

To fulfil global energy needs and protect the environment, reducing fossil fuel use and increasing clean energy sources like hydrogen is essential. Hydrolysis of sodium borohydride offers a safe and cost-effective method for hydrogen production. This study focuses on the use of Ce- and/or Zr-based metal-organic frameworks (MOFs) and their functionalized materials with additives with different levels (5-15 wt%) (ammonium sulfate (AS), ammonium dihydrogen orthophosphate (ADHP), and phosphomolybdic acid (PMA)) as catalysts for the dehydrogenation of $NaBH_4$. These functionalized MOFs exhibit improved catalytic activity compared to the MOFs. 15 wt% AS/NH_2-UiO-66 displayed the highest hydrogen generation rate (377.8 mL H_2 g^{-1} min^{-1}). This study is the first to use Ce-BDC MOF (Ce-UiO-66) as a catalyst in $NaBH_4$ hydrolysis. It produced 75 mL H_2 within 15 min where the functionalized Ce-UiO-66 with 15 wt% ADPH achieved complete hydrolysis in just 9 min. various factors affecting the reaction, such as catalyst mass, $NaBH_4$ concentration, and reaction temperature were analyzed. XRD, FTIR, XPS, BET analysis was used to characterize these catalysts. The acidity of the functionalized MOFs, was assessed using pyridine as a probe. The rate constant, activation energy, enthalpy change, entropy change, and free energy of activation were estimated. These materials could pave the way for more effective catalysts in energy-related applications.

Keywords: MOFs; Ammonium sulfate; Ammonium dihydrogen orthophosphate; Phosphomolybdic acid; Hydrogen generation

1. Introduction

The major concern in our modern society is the production of large amounts of energy with minimal global pollution [1]. The utilization of fossil fuels has a significant negative impact on the environment. Thus, it has become necessary to decrease their consumption and develop "clean" energy sources to reduce this significant global issue [2]. Hydrogen gas is considered an ideal clean and renewable energy resource due to its high energy density, zero emissions, and availability from various sources [3]. The multiple resources for hydrogen production are divided into two groups. The first group includes water-splitting technologies such as water electrolysis [4], photoelectrolysis [5] and thermolysis [6]. The second group contains biomass technologies such as biological processes [7], and thermochemical processes [8]. Recently, hydrolysis of hydrides such as sodium borohydride (NaBH4) has been widely used to generate hydrogen [9,10]. Sodium borohydride (NaBH4) has many advantages, including safety, affordability, relatively high stability, and containment of 10.6 wt% of hydrogen. The hydrolysis of NaBH4 can be elucidated by the following equation:

$$NaBH_4+2H_2O \rightarrow 4H_2+NaBO_2 \quad (1)$$

Δ **H= -212.1 kJ/mol**

Metal-organic frameworks (MOFs) represent a type of porous materials that have adjustable pore size and high surface area [11-16]. They are being increasingly used in various applications, such as catalysis [17-19], sensing [20], biosensing [21], adsorption [22, 23], devices [24, 25], medicine [26,27], drug delivery [28], and photocatalysis. MOFs have been utilized as catalysts in the process of photocatalytic H_2 generation from water [29]. They offer numerous benefits such as a large surface area, substantial pore volume, low density, and various crystal structures, and being easily functionalized with different reagents and conjugated with nanomaterials. Accordingly, they have garnered considerable attention as catalyst for hydrogen generation via NaBH4 hydrolysis [30-34].

In recent years, the addition of sulfate, phosphate, or phosphomolybdic hetero-poly acid has been explored as a promising strategy for improving the properties of MOFs and expanding their applications [35-41]. Such a modification of MOFs may be undertaken either during their direct synthesis [35] or post-synthesis [36, 37]. However, the post-synthesis mode is more commonly used due to its simplicity and versatility.

Because of the marvelous properties of Ce and Zr based MOFs, they have been used in many different applications like photocatalytic hydrogen generation [42-44], and hydrogen production from plastics [45]. In this investigation, the dehydrogenation of $NaBH_4$ was the test reaction used to evaluate the catalytic activity of the Ce- and Zr-MOFs based catalysts. Herein, we added various amounts (5, 10 or 15 wt%) of ammonium sulfate, ammonium dihydrogen orthophosphate, or phosphomolybdic acid to enhance the catalytic conduct of laboratory synthesized MOFs in the dehydrogenation process of

*Corresponding author e-mail: ahmed_abdo@aun.edu.eg.; (Ahmed Abdo Hassan).
Receive Date: 21 July 2024, Revise Date: 28 August 2024, Accept Date: 21 September 2024
DOI: 10.21608/ejchem.2024.306056.10057

$NaBH_4$. The hydrogen generation rate (HGR) values were estimated to understand the role of the acidic nature in affecting the catalytic performance of the catalysts. The acid-functionalized MOFs were found to exhibit higher HGR than the pure MOFs.

2. Experimental details

2.1. Materials

2.1.1. Pure MOFs

UiO-66 (Universitetet i Oslo) (denoted MOF-I) was synthesized as reported by Abdulhamid [46]. Accordingly, 1.808 g of hydrated zirconyl chloride (ZrOCl2.8H2O), 0.987 g of terphthalic acid (Benzene 1,4-dicarboxylic acid (BDC) = C6H4(CO2H)2), and 5.3 mL of acetic acid (C2H4O2) were mixed in 120 mL of dimethylformamide (DMF) and sonicated for 30 min. The resulting solution was placed into a 250-mL Teflon-lined stainless steel autoclave and heated at 120 oC for 24 h. After cooling to room temperature (RT), the yielding white precipitate was separated, washed with DMF (120 mL) and ethanol (120 mL), and dried at 85 oC in an electric oven overnight. NH2-UiO-66 (denoted MOF-II) was synthesized, washed, and dried adopting the same recipe [46], however using 1.07 g of 2-amino terphethalic acid (2-aminobenzene 1,4-dicarboxylic acid (NH2-BDC) = (NH2)C6H4(CO2H)2) instead of BDC.

On the other hand, Ce-UiO-66 (Ce-BDC MOF) (*denoted* MOF-III) was synthesized by adopting the recipe reported by Yasssin and Taddesse [47]. Accordingly, a solution was made by dissolving a 1.644 g of cerium (IV) ammonium nitrate in 3.6 mL of distilled water and stirring for 30 min. Subsequently, a second solution was made by dissolving a 0.332-g portion of terphethalic acid (BDC) in 15.4 mL DMF. Then, the second solution was added stepwise onto the first solution to form a yellow precipitate of Ce-UiO-66. The precipitate was stirred at RT for 24 h, separated by centrifugation, washed three times by DMF and acetone, and dried at 80 ^oC overnight.

2.1.2. Acid-functionalized MOFs

The thus synthesized pure MOFs were functionalized by the impregnation of three different acidic additives, namely ammonium sulfate (AS = $(NH_4)_2SO_4$), ammonium dihydrogen orthophosphate (ADHP = $NH_4H_2PO_4$), and phosphomolybdic acid (PMA = $H_3PMo_{12}O_{40}$). A general wet impregnation method, similar to that reported in the literature [48], was performed for MOF-I, MOF-II, or MOF-III.

2.1.2.1. Synthesis of x PMA/MOF

PMA/MOFs were synthesized by wet impregnation. 1g of MOF was added to an aqueous PMA solution containing the desired amount of PMA (where x= 5, 10, 15 wt%), followed by stirring for approximately 2 hours at 70°C. The resulting mixture was then dried in an oven at 100°C for 24 hours.

2.1.2.2. Synthesis of x ADPH/MOF

ADPH /MOFs were prepared via the wet impregnation method [48]. MOF was mixed with calculated amounts of $NH_4H_2PO_4$ (ADPH) (5, 10, 15 wt%) dissolved in a small quantity of distilled water. The mixture was stirred for 2 hours at 70°C and subsequently dried in an oven at 100°C for 24 hours.

2.1.2.3. Synthesis of x AS/MOF

AS/MOFs were synthesized by the wet impregnation method, using different amounts of $(NH_4)_2SO_4$ (5, 10, 15 wt%). For instance, 5AS/MOF-I indicates a 5 wt% sulfate-impregnated Zr-based MOF, whereas 15PMA/MOF-III indicates a 15 wt% phosphomolybdic acid-impregnated Ce-based MOF.

It is worth noting, that all of the chemicals employed in the material synthesis course were ≥ 99% pure products of either Alfa Aesar or Sigma-Aldrich, and used as obtained.

2.2. Characterization techniques

The bulk and surface compositions of the pure and functionalized MOFs were characterized by X-ray diffractometry (XRD), Fourier-transform infrared spectroscopy (FTIR), and X-ray photoelectron spectroscopy (XPS). XRD diffractograms were acquired (at 5-90^o, 0.06^o/min, and λ = 1.5418 Å) employing a model PW 2103100 Philips diffractometer. FTIR spectra were taken (at 4000-400 cm^{-1} and a resolution of 4 cm^{-1}) from lightly loaded disks of KBr-supported test samples on a Shimadzu IR-470 spectrophotometer (Japan). XPS spectra were recorded using a Thermo VG Scientific spectrometer. The radiation source was monochromatic AlKα radiation power 1486.6 eV, the vacuum in the analysis chamber was better than 1 x 10^{-9} bar, and the binding energy (BE/eV) determination was based on the carbon contamination C1s at 284.6 eV. Nitrogen adsorption was used for estimating BET surface areas of the prepared catalysts. Quantachrome (model 3200) gas adsorption apparatus was used for constructing the nitrogen adsorption-desorption isotherm of the catalysts (0.1 gm). Pyridine chemisorption measurements were carried out on test MOFs, by first exposing portions of the MOFs to pyridine vapor inside pre-evacuated desiccators containing an aliquot of liquid pyridine at RT overnight. Then, a weighted amount of the pyridine-covered MOF was subjected to thermal analysis. Eventually, the numbers of chemisorbed pyridine molecules were determined and used to gauge the MOF surface acidity.

2.3. Catalytic activity evaluation

2.3.1. Catalysis measurements

In a 100 mL flask, NaBH4 was hydrolyzed and the volume of the evolving H2 gas (VH2/mL) was measured as a

function of time (t/min) under isothermal conditions, using gasometry measurements. The VH2 was determined concerning the volume of water displaced from the liquid burettes attached to the flask system. This allowed the pressure on both sides of the manometer to be equalized. The flask was placed in an ultra-thermostat, which automatically controlled the reaction temperature (30-45 oC) with the help of a magnetic stirrer to maintain a constant temperature. Typically, 50 mL of an aqueous solution of the borohydride of a given concentration (0.03-0.07 M) was poured into the flask and a given mass (0.03-0.07 g) of the test catalyst was added to trigger the reaction. The volumes were recorded at different time intervals (up to 30 min). The results obtained enabled the construction of isothermal VH2-t plots for each run. It is worth noting, however, that immediately before testing the catalytic activity of the MOFs they were mildly activated by heating at 80-100 oC for 1 h.

2.3.2. Data processing for kinetic and thermodynamic parameters

The obtained VH2-t plots were transformed into [NaBH4]-t plots, whereby ln(a-x)-t plots were constructed and the reaction (n) was determined applying the try-and-error algorithm. The reaction rate constant (k) was then derived from the slope of the linear ln (a-x)-t plots. The effect of reaction temperature (T/K) on the rate constant value made possible the application of Arrhenius equation (2) and, hence, the construction of linear ln k-T-1 plots, whereby derivation of values of the pre-exponential parameter (A) and the activation energy (Ea/kJ.mol-1) was enabled.

$$\ln k = \ln A - Ea/RT \quad (2)$$

The enthalpy (ΔH/kJ.mol-1) and entropy (ΔS/kJ.mol-1) changes accompanying the catalytic reaction were calculated by applying the Erying equation (3):

$$k = kBT/h\, e^{\Delta S/R}\, e^{-\Delta H/RT} \quad (3)$$

Where, k, kB and h are the rate constant, Boltzmann constant (1.381 X 10-23 J/K), and Plank's constant (6.626 x10-34 J.s). Accordingly, the free energy change (ΔG/kJ.mol-1) accompanying the reaction was calculated using the thermodynamic relationship given in equation (4):

$$\Delta G = \Delta H - T\Delta S \quad (4)$$

3. Results and discussion

3.1. Bulk phase and chemical composition for the MOFs

The X-Ray diffractograms obtained for the pure and functionalized MOFs are stacked in Fig. 1-(a-c). Pure MOF-I-III are shown to recognizably exhibit two strong diffraction peaks at 2θ = 7.08-7.26° and 8.20-8.32°, and five weak peaks at 24.83-25.56°, 29.67-30.35°, 42.14-42.4°, 50.13-50.43°, and 57.18-57.51°. This diffraction pattern indicates that the reflecting atomic arrays are due to crystallites of Zr(IV)-terephthalate metal-organic frameworks as compared to the JCPDS File No. 00-451-2072 [49]. Accordingly, one may suggest that the Ce-content of MOF-III did neither influence the buildup of the basic Zr-based MOF nor segregate into an XRD-detectable crystalline phase. However, the possibility of the formation of quite isomorphous Ce(IV)-terephthalate MOF cannot be excluded with certainty. The diffractograms obtained for variously acid-functionalized MOFs (Fig. 1-(a-c) also show that irrespective of the MOF used, neither of the three acid additives (i.e., AS, ADHP, nor PMA) did influence significantly the diffraction patterns observed for the pure MOFs. This may help suggest that the additive species are highly dispersed into the MOF pores in, most likely, a non-crystalline form

.

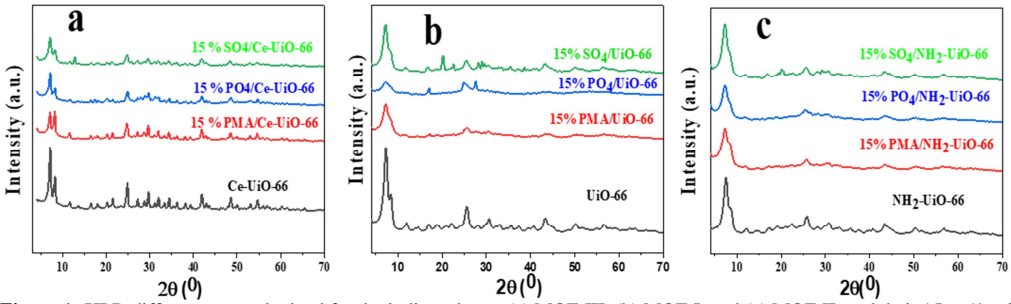

Figure 1: XRD diffractograms obtained for the indicated pure (a) MOF-III, (b) MOF-I, and (c) MOF-II, and their 15 wt% acid-functionalized versions.

Bulk chemical compositions of the pure and functionalized MOFs were characterized using FTIR spectroscopy; the spectra obtained are displayed in Fig. S1. The in-set spectra obtained for pure BDC (Fig. S1-a and S1-b) and NH_2-BDC (Fig. S1-c) are shown to monitor the following diagnostic absorptions (i) 3510-3500 cm^{-1}, (ii) 3400-3390 cm^{-1}, (iii) 1660 cm^{-1}, (iv) 1505-1495 cm^{-1}, (v) 1588-1561 cm^{-1} and 1394-1384 cm^{-1} due to νNH_2, O-H stretching , ν(C=O) , ν(C=C) in benzene ring and asymmetric and symmetric peaks of stretching modes of carboxylic groups [50-55]. Except for the absorptions due to νNH_2, which are only observed in the spectrum of NH_2-BBDC (Fig. S1-c), the other absorptions are monitored in the spectra of the pure parent materials BDC and NH_2-BDC.

For the functionalized MOFs, the following diagnostic absorptions can be observed in the spectra. The absorptions at 1065 cm^{-1}, 965 cm^{-1}, 868 cm^{-1} and 785 cm^{-1} are respectively attributed to νP-O, νMo=O, νMo-O_b-Mo and νMo-O_c-Mo vibrations [56-58] of PMA in 15PMA/MOFs , whereas the absorptions at 1115-1040 cm^{-1}, 1020-1010 cm^{-1} and 520 cm^{-1} are assignable to various vibrations of PO_4 [59-61] in 15ADHP/MOFs. On the other hand, the absorptions at 1108 cm^{-1}, 660-650 cm^{-1}, and 620-610 cm^{-1} are due to SO_4 vibrations [62-64] of AS in 15AS/MOFs. Moreover, the sharp absorption at 1385 cm^{-1} only monitored in the spectra of MOF-II (Fig. S1-c) is indicative of νNO_3^- ionic species, which are inherited during the preparation course of MOF-III. Monitoring of these absorptions in the IR spectra obtained for the test pure and functionalized MOFs evidences the anticipated chemical makeup of the yielding materials.

3.2. Surface elemental constitution and Texture investigation of pure and functionalized MOF-II

3.2.1. Surface elemental constitution of functionalized MOF-II

The fact that the various acid-functionalized MOF-II materials exhibited relatively high catalytic activity (*vide infra*) rendered their XPS examination worth doing. The survey and high-resolution (HR) XPS spectra obtained for 15AS/MOF-II, 15ADHP/MOF-II, and 15PMA/MOF-II are displayed in Figs. 2, S2 and S3, respectively. The survey XPS spectrum obtained for 15AS/MOF-II monitors electron emission peaks due to Zr 3d, S 2p, N 1s, C 1s, and O 1s (Fig. 2-a). The HR-XPS spectrum of Zr 3d (Fig. 2-b) shows two peaks at B.E.values of 182.6 and 185.2 eV corresponding to Zr $3d_{5/2}$ and Zr $3d_{3/2}$, respectively [52,65-68]. The 2.6-eV difference between them indicates that the source Zr is in the 4+ oxidation state. The HR-XPS of S 2p shows two peaks at 168.4 and 169.69 eV corresponding to $S2p_{3/2}$ and $S2p_{1/2}$, respectively, which can be related to structural sulfate (Fig. 2-c) [69]. The presence of nitrogen atoms was confirmed by two peaks at 399.05 and 401.13 eV corresponding to N-H and C=N, respectively (Fig. 2-d) [65]. The HR-XPS of C 1s resolves three peaks at 284.49, 286.05, and 288.4 eV referring to C=C, C-N, and O-C=O (Fig. 2-e), respectively [52,70,71]. The HR-XPS of O 1s shows three peaks at 530.03, 531.5, and 532.4 eV corresponding to Zr-O, Zr-OH, and sulfate-oxygen, respectively (Fig. 2-f).

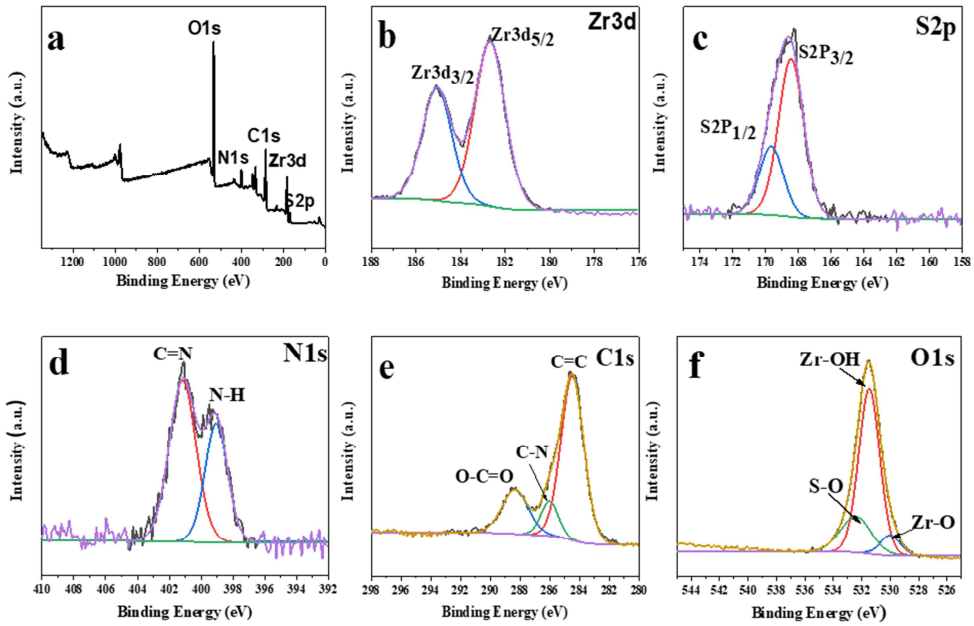

Figure 2: Survey (a) and HR-XPS (b-f) spectra obtained for 15AS/MOF-II.

XPS spectra obtained for 15ADHP/MOF-II are presented in Fig. S2. The survey spectrum (Fig. S2-a) monitors peaks indicative of Zr 3d, P 2p, N 1s, C 1s, and O 1s electron emission sources. The HR-XPS of Zr 3d shows the two peaks (at B.E. = 182.9 eV and 185.3 eV) diagnosing the exposure of Zr^{4+} (Fig. S2-b) [52, 65-68]. Fig. S2-c shows the HR-XPS of P 2p with one peak at 133.4 eV confirming the presence of PO_4^{-3} species [66, 68, 72]. Conversely, the HR-XPS for N 1s peak deconvolution resolves two peaks at 398.7 and 401.2 eV assignable to N-H and C=N, respectively (Fig. S2-d) [68]. The carbon C 1s shows three peaks at 284.46, 285.99, and 288.46 eV referring to C=C, C-N, and O-C=O, respectively (Fig. S2-e) [52, 70,71]. O 1s peak analysis resolves three peaks at 529.85, 531.43 and 532.76 eV assignable to Zr-O, P-O-Zr and P–O–H, respectively (Fig. S2-f) [73].

Fig. S3 demonstrates the XPS spectra obtained for 15PMA/MOF-II. The survey spectrum (Fig. S3-a) reveals the presence of P 2p and Mo 3d, in addition to the expected Zr 3d, O 1s, N 1s and C 1s emission sources. Deconvolution of the Zr 3d peak resolves the two peaks (at 182.86eV and 185.32 eV) attributable to the Zr 3d5/2 and Zr 3d3/2 emissions (Fig. S3-b) of Zr^{+4} [52, 65-68]. Fig. S3-c shows one peak at 133.5 eV related to P=O [74]. N 1s peak analysis (Fig. S3-d) resulted in three peaks at 398.2, 399.25 and 400.48 eV corresponding to N-C, $-NH_2$, $-NH_3^+$, respectively [70]. The C 1s peak analysis (Fig. S3-e) also results in shows three peaks (at 284.78, 286.2, and 288.48 eV) but referring to C=C, C-N, and O-C=O, respectively [52, 70,71]. Uniquely, the Mo 3d peak analysis resolved two peaks at 232.57 and 235.79 eV corresponding to Mo $3d_{5/2}$ and Mo $3d_{3/2}$, respectively (Fig. S3-f) [74] in oxidation state 6+.

3.2.2. Texture investigation of pure and functionalized MOF-II

The adsorption isotherms of some selected samples from the prepared MOFs under investigation were measured at liquid nitrogen temperature (-196^{0}C) and the calculated S_{BET} values for these samples were tabulated in Table 1.

Table (1): S_{BET} values pure and functionalized MOF-II

Catalyst	S_{BET}
NH_2-UiO-66	130.8
15% PMA/ NH_2-UiO-66	35.4
15% PO_4/ NH_2-UiO-66	48.87
15% SO_4/ NH_2-UiO-66	85.84

Summing up, the above presented and described characterization results may help draw the following implications: (i) the pure and acid-functionalized MOFs only contain a single crystalline phase (Zr^{4+}-phethalate), whereas the rest of the components of their chemical make are either highly dispersed into pores of the crystalline MOFs' structure, or non-crystalline; (ii) the impregnated parent materials (AS, ADHP, or PMA) of the acidic species are loaded by mechanical deposition, thus showing no mutual interaction with the MOF composition; (iii) the expected elemental constitution of the test MOFs is exposed at the surface, which may imply that the acid additives do not cover-up the metal content (Zr) of the test MOF, and neither of the acid additives could change the zirconium oxidation state (4+).

3.3. Sodium borohydride dehydrogenation activity

3.3.1. Gasometry of hydrogen generation

Fig. 3 compares V_{H2}-t plots obtained via gasometry data measured during the dehydrogenation reaction of aqueous solutions of $NaBH_4$ (50 mL, 0.05 M) at 30 ^oC in the presence of the test catalyst (0.05 g-Cat). The plots are shown to assume an initial linearity followed by a subsequent downward deviation. The initial linearity accounts for a linear increase in the hydrogen generation rate (HGR) that is catalyst surface dependent (i.e., zero-order kinetics). However, the subsequent non-linearity accounts for a slowing HGR that is reactant concentration rate dependent (i.e., 1st order kinetics). Furthermore, (i) the activity of the three pure MOFs is shown to improve upon functionalization with AS, ADHP and PMA, and (ii) the test catalysts can be arranged according to the following activity ascending order: pure MOF<PMA-<AS-≤ADHP-functionalized MOF (at 15 wt% level), irrespective of the MOF used (i.e., MOF-(I-III).

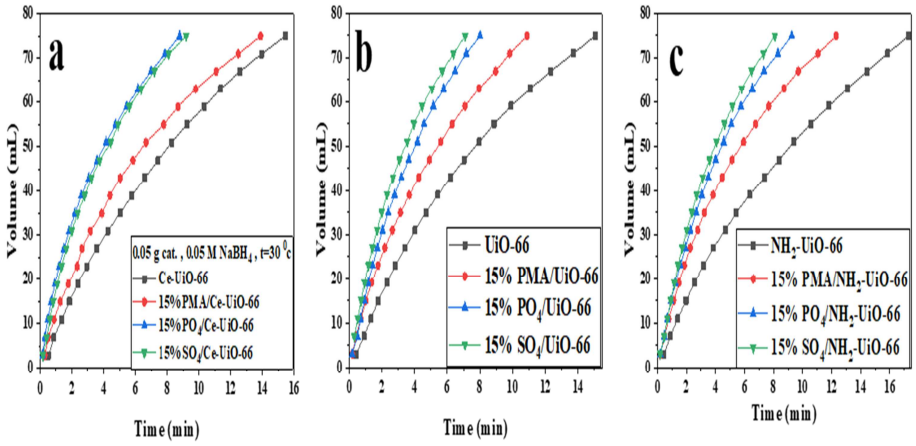

Figure 3: V_{H2}-t plots obtained in the presence of the indicated pure and functionalized MOFs under the following invariant reaction conditions: 50 mL of $NaBH_4$ solution (0.05 M), test catalyst mass (0.05 g), and reaction temperature (30 ^oC)

The above findings are consolidated by the histograms exhibited in Fig. S4, which reveal the decrease of the duration necessary to generate 75 mL of H_2 (V_{75}) upon increasing the loading level (from 5 up to 15 wt %) of AS or ADPH, irrespective of the MOF used. Accordingly, the importance of surface acidity to the dehydrogenation activity can be inferred.

3.3.2. Influence of reaction variables

3.3.2.1 Catalyst mass

Scanning of the effect of catalyst mass (0.05-0.07 g) was conducted using 0.05 M $NaBH_4$ solution at 30 ^0C. V_{H2}-t plots thus obtained are compared in Fig. 4. The figure indicates that the time required to produce V_{75} of H_2 is decreased upon increasing the catalyst amount. This observation reveals that the dehydrogenation activity increases with the catalyst mass (i.e., surface area).

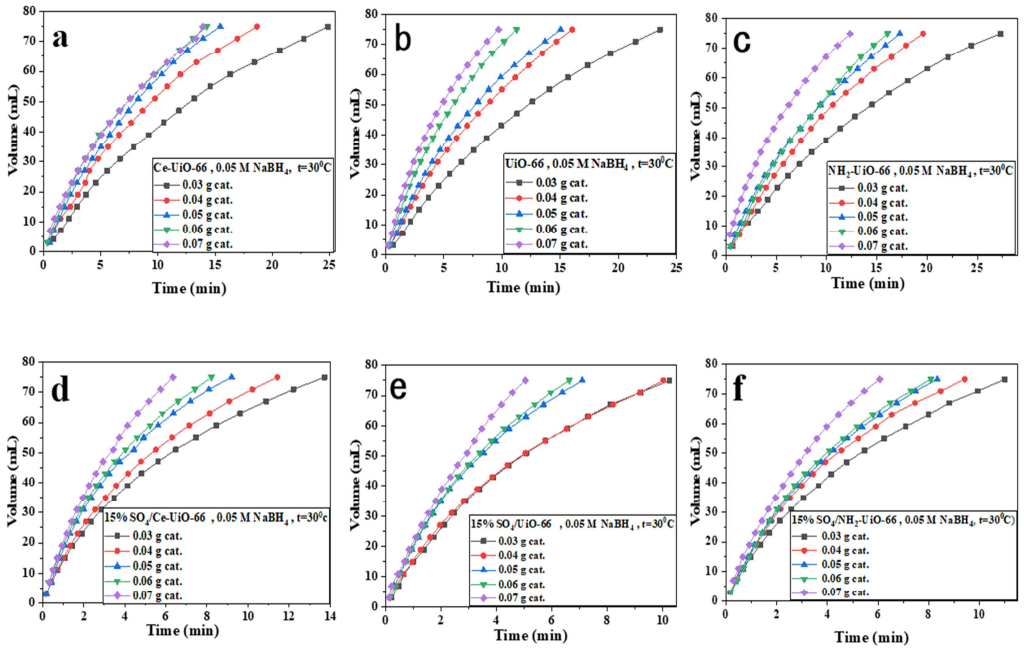

Figure 4: V_{H2}-t plots obtained to test the influence of the catalyst mass (0.05-0.07 g) in the presence of the indicated pure and AS-functionalized MOFs under the following invariant reaction conditions: 50 mL of $NaBH_4$ solution of 0.05 M; and reaction temperature (30 ^oC).

3.3.2.2 $NaBH_4$ concentration

V_{H2}-t plots obtained (Fig. 5) indicate that the time required to generate V_{75} of H_2 decreases upon increasing the borohydride concentration on a given catalyst. In other words, increasing the reactant concentration is shown to increase the dehydrogenation activity. This may reflect that the dehydrogenation reaction is 1st-order kinetically controlled, particularly at the long-time regime.

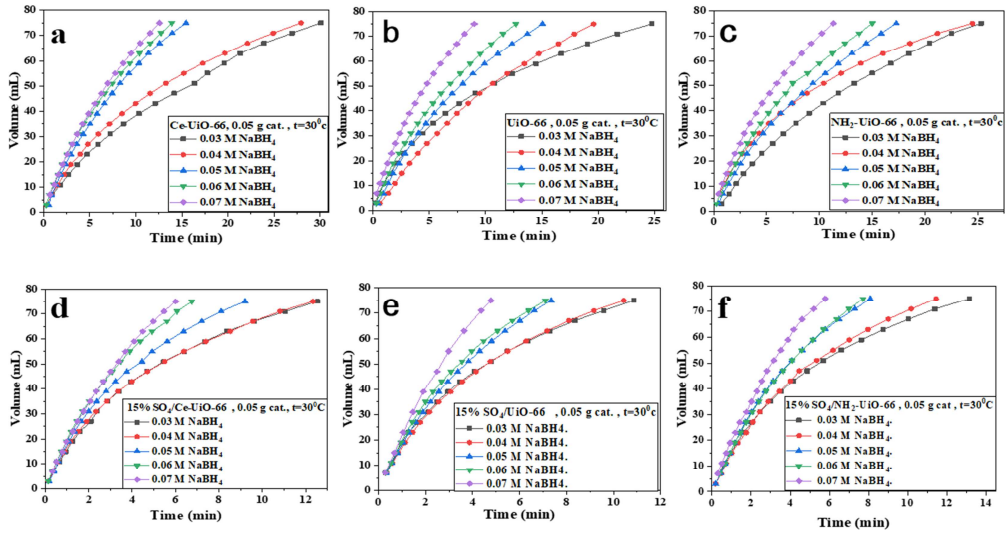

Figure 5: VH2-t plots obtained to test the influence of the NaBH4 concentration (0.03-0.07 M) in the presence of the indicated pure and AS-functionalized MOFs under the following invariant reaction conditions: 50 mL of NaBH4 solution; catalyst mass (0.05 g); and reaction temperature (30 oC).

3.3.2.3. Reaction temperature

V_{H2}-t plots scanning the influence of the reaction temperature are displayed in Fig. S5. The results communicated highlight the direct relationship between the reaction temperature and HGR.

3.4. Catalytic dehydrogenation kinetic and thermodynamic parameters

To calculate the catalytic dehydrogenation kinetic and thermodynamic parameters, we have performed the following processing of the gasometry data: (i) the V_{H2}-t plots were converted to ln(a-x)-t plots; (ii) ln(a-x)-t data obtained as a function of reaction temperature (30-45 ^{o}C) were subjected to linear regression analysis (Fig. 6) in order to verify the 1st-order kinetics of reaction, whereas the rate constant values (k/min) were determined as a function of reaction temperature (T/K) (Table 2); (iii) adopting equation (2), Arrhenius plots (ln(k)-(1/T) were constructed (Fig. 7), and the reaction activation energy values (ΔE_a/kJ mol^{-1}) (Table 2) were derived from values of their slopes; (iv) the rate constant values were processed applying the algorithm of equation (3) to calculate the reaction enthalpy (ΔH/kJ mol^{-1}) and entropy (ΔS/kJ mol^{-1}) changes (Table 2); and (v) with the help of equation (4) the reaction free energy change (ΔG/kJ mol^{-1}) (Table 2) was calculated.

Inspection of the resulting kinetic and thermodynamic parameters (Table 2), the activation energy values can help arrange the test catalysts in the following activity descending order: 15AS/MOF-II≥15AS/MOF-I>MOF-I>15AS/MOF-III>MOF-III≥MOF-II. Thus, the AS-functionalization of the MOFs promotes its dehydrogenation activity toward $NaNH_4$ in solution. Moreover, MOF-I is relatively more active than the other pure MOFs (i.e., MOF-II and MOF-III).

The pyridine-gauged surface acidity results (Fig. 8) can justify the following correlations: (i) the surface acidity of the pure MOFs is arranged in the following descending order: MOF-I>>MOF-III≥MOF-II; (ii) on MOF-I or MOF-III, the surface acidity generated as a function of the added acidic species is arranged in the following descending order: 15ADHP>15PMA≥15AS, whereas on MOF-II, it is arranged in the following descending order: 15PMA>15ADHP≥15AS; (iii) for AS or ADHP acidic species, the surface acidity as a function of the pure MOF used is arranged in the following descending order: MOF-I>MOF-III>MOF-II, whereas for PMA acidic species, the descending order is rendered: MOF-I>MOF-II≥MOF-III. When these acidity descending correlations are compared with the above-mentioned activity descending correlation, one may infer the following: (i) the catalytic dehydrogenation activity of pure MOFs is largely dependent on the surface acidity, and (ii) the impregnation of acidic species (AS, ADHP, or PMA) promotes the activity of the pure MOFs.

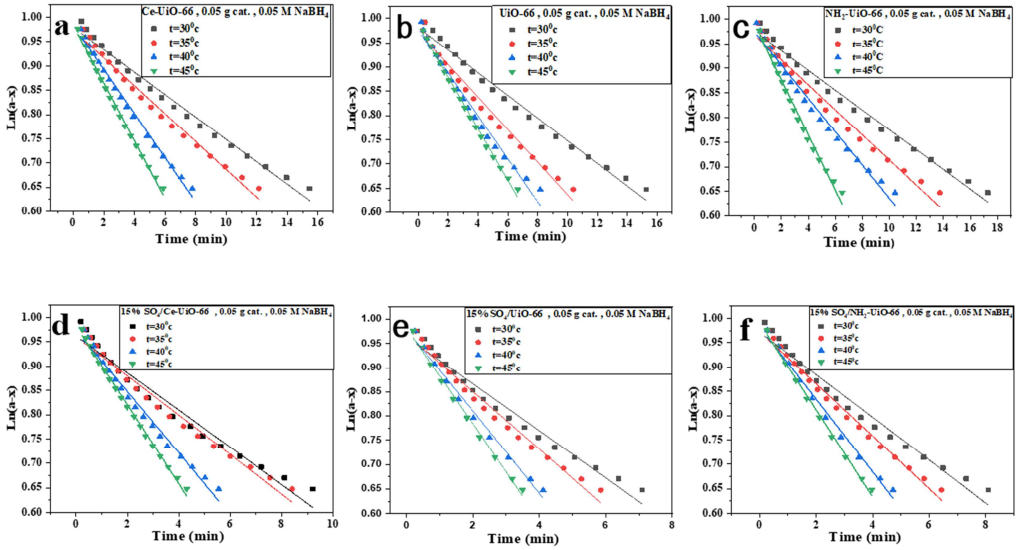

Figure 6: ln (a-x) versus time plots constructed for the $NaBH_4$ dehydrogenation reaction on the indicated pure and acid-functionalized MOFs at different reaction temperatures (30-45^{0}C).

The results given in Table (2) reveal, moreover, that the calculated ΔG and ΔH assume negative values, whereas ΔS assumes positive values. Furthermore, the ΔG and ΔS values increase with reaction temperature (Table 2). This indicates that the catalytic dehydrogenation of $NaBH_4$ on the test MOFs is thermodynamically feasible. It is to be inferred from Table 2 that the AS-functionalization of the pure MOFs at 15 wt% is the proper choice to promote the catalytic conduct of the test MOFs.

Table (2): Calculated kinetic and thermodynamic parameters

Catalyst	T (K)	K(min^{-1})	K(sec^{-1})	Ea (KJ)	ΔH (KJ)	ΔS (KJ)	ΔG (KJ)
Ce-UiO-66	303	0.023	0.00039	52.73	-212	1.01	-94.022
	308	0.029	0.00048	52.73	-212	0.997	-95.084
	313	0.045	0.00075	52.73	-212	0.982	-95.508
	318	0.059	0.00099	52.73	-212	0.97	-96.342
15% SO_4/Ce-UiO-66	303	0.038	0.00063	47.73	-212	1.006	-92.814
	308	0.040	0.00067	47.73	-212	0.994	-94.230
	313	0.063	0.00105	47.73	-212	0.980	-94.632
	318	0.081	0.00135	47.73	-212	0.967	-95.522
UiO-66	303	0.023	0.00039	44.01	-212	1.01	-94.022
	308	0.0234	0.00056	44.01	-212	0.996	-94.689
	313	0.031	0.00074	44.01	-212	0.983	-95.543
	318	0.053	0.00088	44.01	-212	0.971	-96.653
15% SO_4/UiO-66	303	0.048	0.00081	40.07	-212	1.003	-92.181
	308	0.059	0.00099	40.07	-212	0.991	-93.230
	313	0.085	0.00141	40.07	-212	0.977	-93.865
	318	0.099	0.00165	40.07	-212	0.965	-94.991
NH_2-UiO-66	303	0.020	0.00034	53.67	-212	1.011	-94.368
	308	0.024	0.00040	53.67	-212	0.999	-95.550
	313	0.029	0.00049	53.67	-212	0.986	-96.616
	318	0.042	0.00070	53.67	-212	0.973	-97.258
15% SO_4/NH_2-UiO-66	303	0.044	0.00073	39.37	-212	1.005	-92.443
	308	0.054	0.00090	39.37	-212	0.992	-93.474
	313	0.075	0.00124	39.37	-212	0.978	-94.200
	318	0.089	0.00149	39.37	-212	0.966	-96.261

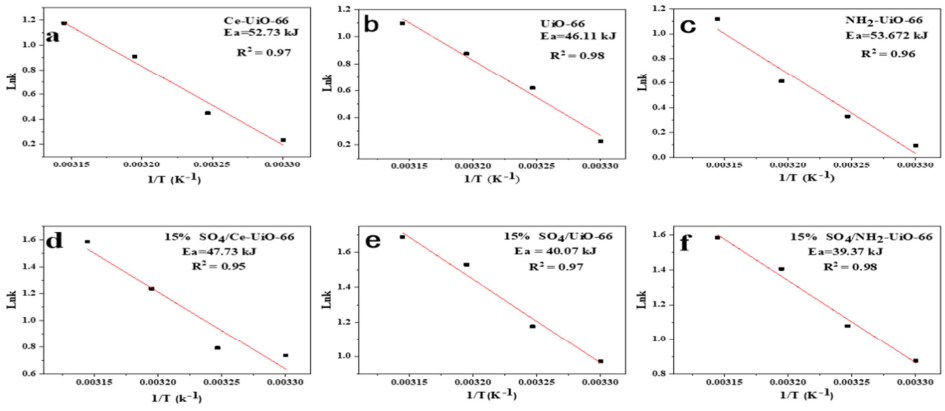

Figure 7: Arrhenius plots (ln k versus 1/T) constructed for the NaBH4 dehydrogenation reaction the pure and acid-functionalized MOFs.

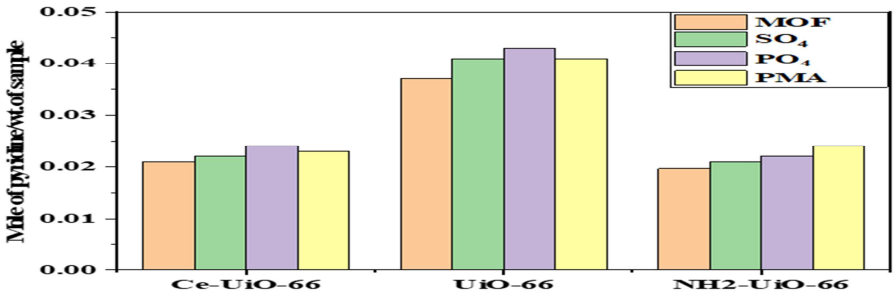

Figure 8: Histograms representing the acidity of pure and 15%functionalized MOFs

3.4. Reaction mechanistic aspects

Literature discussions about the mechanistic pathway of the catalytic dehydrogenation of $NaBH_4$ in aqueous solution are focused on a stepwise process including the formation of $B(OH)_4^-$ as the main intermediate via $B(OH)_3$ [75].

$$B(OH)_3\ (aq) + H_2O_{(l)} \leftrightarrow B(OH)_4^-(aq) + H^+ \quad (5)$$

Recently, the above reaction has been considered [76] to commence with the formation of a short-living $BH_3(OH)^-$ as has been suggested to occur throughout the following stepwise sequence:

$$BH_4^- \rightarrow BH_3(OH)^- \rightarrow BH_2(OH)_2^- \rightarrow BH(OH)_3^- \rightarrow B(OH)_4^- \quad (6)$$

The hydrolysis kinetics of $NaBH_4$ over various catalysts has been suggested to follow different models [77-90]. Accordingly, our present synthesized catalysts expose acid sites (Bronsted and/or Lewis type) that can serve as active centers for the hydrolysis of $NaBH_4$. Ce and/or Zr MOFs and their functionalized versions expose the Zr_6 node with fully reversible hydroxylation groups [91]. The total amount of the acid sites exposed on our catalysts was determined by pyridine chemisorption experiments (Fig. 8). Furthermore, the Zr node has a flexible coordination geometry for Zr^{4+}. Consequently, it is possible to access the presence of both the hydroxylated and dehydroxylated forms. This also may allow for an amphoteric character, i.e., acid–base pair properties [92,93].

Accordingly, a reaction mechanism over the present catalysts can be proposed to involve the following adsorptive and catalytic events:

(i) Dissociative adsorption of H_2O molecules on acid sites to form H^+ and OH^- ions; (ii) adsorption of BH_4^- on the adjacent base site leading to the formation of BH_3 and H^- Then, Both H^+ and H^- combine to form H_2 molecules; (iii) The resulting OH^- and BH_3 combine to form $BH_3(OH)^-$, and the reaction propagates in a stepwise fashion till the formation of $B(OH)_4^-$ as the stable reaction intermediate. Similar mechanistic steps were reported for $NaBH_4$ [94].

Therefore, the desired proposed mechanism goes parallel with that suggested by Langmuir –Hinshelwood and Michalis-Menten mechanisms [77].

3.5. Catalyst recyclability

To assess the recyclability, the catalyst 15AS/MOF-III was employed for long-term hydrogen (H_2) generation. Fig. 9-a presents the outcomes of multiple cycles of H_2 generation through the hydrolysis of $NaBH_4$ catalyzed by this catalyst, which was reused without any modification. The hydrolysis reaction was performed at 30°C with 0.05 M of $NaBH_4$ and 50 mg-Cat. As shown in Fig. 9-a, the HGR was slightly changed throughout four cycles. These findings indicate that the catalyst can be reused effectively because their catalytic activities exhibit consistent behavior with minimal alterations. The XRD pattern of the catalyst after four cycles (Fig. 9-b) proved that the catalyst can be regenerated.

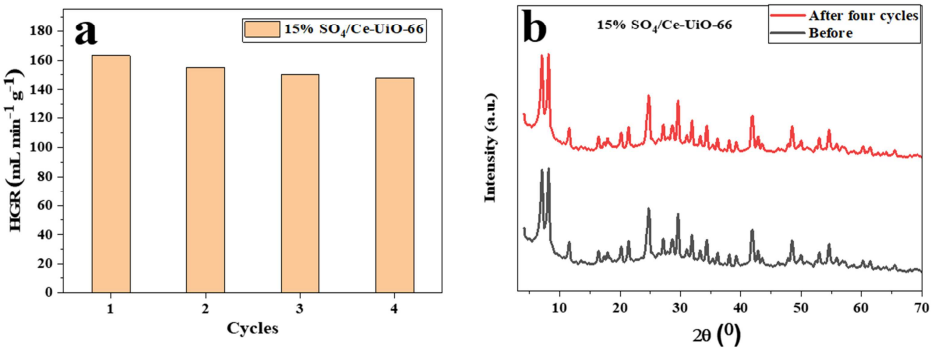

Figure 9: a) Recyclability effect on the performance of 15AS/MOF-III catalyst, b) XRD of 15AS/MOF-III catalyst before and after four cycles.

Table 3 compares HGR values measured on our present catalysts with reported previously. 15% SO_4/UiO-66, 15% SO_4/ NH_2-UiO-66, 15% PO_4/ UiO-66 and 15% PO_4/Ce-UiO-66 give higher HGR values than other catalysts. They exhibited 211.3, 185.6, 177.1 and 170.8 $mL.min^{-1}.g^{-1}$ in 0.05 M NaBH4 at reaction temperature 30 ^{0} C. The comparison reveals that our catalysts are quite competitive and even superior to the reported catalysts such as ZrOSO4/C-10wt. %H2SO4 [22]. ZrOSO4/C-50 wt.%H_2SO_4 [22]. 5.4 wt.% Ru/Al_2O_3 [77], Ni [78], Co-B/C [79] and Co/MWCNTs-2 [80].

Table 3: HGR values measured using our present catalysts and literature-reported ones.

Catalyst	Catalyst wt.	Reaction conditions	HGR ($mL.min^{-1}.g^{-1}$)	Ref.
$ZrOSO_4$/C-10 wt.%H_2SO_4	100 mg	0.19 wt. % $NaBH_4$, room temperature	12.5	[36]
$ZrOSO_4$/C-10 wt.%H_2SO_4	100 mg	0.34 wt. % $NaBH_4$, room temperature	19	[36]
$ZrOSO_4$/C-10 wt.%H_2SO_4	100 mg	1 wt. % $NaBH_4$, room temperature	100	[36]
$ZrOSO_4$/C-50 wt.%H_2SO_4	100 mg	0.19 wt. % $NaBH_4$, room temperature	66.5	[36]
5.4 wt.% Ru/Al_2O_3	500 mg	10 wt.% $NaBH_4$, 30 ^{0}C	65.5	[95]
Ni	75%	14 wt.% $NaBH_4$, 30 ^{0}C	96.3	[96]
Co-B/C	2.5%	1 wt.% $NaBH_4$, 5 wt.%NaOH, 25 ^{0}C	166	[97]
Co/MWCNTs-2	15%	1wt.% $NaBH_4$, 35 ^{0}C	109	[98]
Ce-UiO-66	50 mg	0.05 M $NaBH_4$, 30 ^{0}C	97.1	This study
15% PMA/Ce-UiO-66	50 mg	0.05 M $NaBH_4$, 30 ^{0}C	108.1	This study
15% PO_4/Ce-UiO-66	50 mg	0.05 M $NaBH_4$, 30 ^{0}C	170.8	This study
15% SO_4/Ce-UiO-66	50 mg	0.05 M $NaBH_4$, 30 ^{0}C	163.1	This study
UiO-66	50 mg	0.05 M $NaBH_4$, 30 ^{0}C	99.67	This study
15% PMA/UiO-66	50 mg	0.05 M $NaBH_4$, 30 ^{0}C	137.9	This study
15% PO4/UiO-66	50 mg	0.05 M $NaBH_4$, 30 ^{0}C	177.1	This study
15% SO_4/UiO-66	50 mg	0.05 M $NaBH_4$, 30 ^{0}C	211.3	This study
NH_2-UiO-66	50 mg	0.05 M $NaBH_4$, 30 ^{0}C	86.8	This study
15% PMA/ NH_2-UiO-66	50 mg	0.05 M $NaBH_4$, 30 ^{0}C	121.8	This study
15% PO_4/ NH_2-UiO-66	50 mg	0.05 M $NaBH_4$, 30 ^{0}C	162.7	This study
15% SO_4/ NH_2-UiO-66	50 mg	0.05 M $NaBH_4$, 30 ^{0}C	185.6	This study

4. Conclusion

Highly efficient Ce and/or Zr MOFs functionalized with different anions (PO_4^{3-}, SO_4^{2-}, and phosphomolybdic acid) were successfully synthesized via the wet impregnation method. These catalysts were characterized by XRD, FTIR and XPS and evaluated in the dehydrogenation of sodium borohydride in solution. The catalysts provide high efficiency, short time, low catalyst quantity, and low leaching. 15% SO_4/NH_2-UiO-66 showed that a low concentration $NaBH_4$ solution (50 mM) could provide a high hydrogen generation rate (HGR) of 377.83 mL H_2 g^{-1} min^{-1}. The amphoteric nature of the materials due to the coexistence of an acidic base pair that was determined from quantitative measurement of the chemisorption of pyridine ensures high catalytic performance via the hydrolysis of $NaBH_4$. The kinetics and reaction order were studied and the Arrhenius activation energy was found to be in the range of 39-52 KJ/mole. Moreover, the recognized behaviours of entropy, activation energy, enthalpy and free energy declared the spontaneity, feasibility and exothermicity of the hydrolysis reaction. Moreover, the materials display significant recyclability. The catalysts showed excellent activity and reproducibility up to four times without exhibiting much activity making these catalysts promising ones for energy-based applications and can be applied for industrial-scale production. It is expected that this work may provide new avenues for further designing highly efficient and promoted metal-organic frameworks for hydrogen generation via the hydrolysis of $NaBH_4$.

Declaration of competing interest

The authors declare that they have no known competing financial interests or personal relationships that could have appeared to influence the work reported in this paper.

Acknowledgements

This work was financially supported by Assiut University, Egypt.

5. References:

[1] M. Liang , B. Luo , L. Zhi, Application of graphene and graphene-based materials in clean energy-related devices, Int. J. Energy Res. 33 (2009) 1160-1170.
[2] H.Ã. Lund, B.V. Mathiesen, Energy system analysis of 100 % renewable energy systems — The case of Denmark in years 2030 and 2050, Energy 34 (2009) 524–531.
[3] P. Brack, S.E. Dann, K.G.U. Wijayantha, Heterogeneous and homogenous catalysts for hydrogen generation by hydrolysis of aqueous sodium borohydride (NaBH4) solutions, Energy Sci. Eng. 3(3) (2015) 174–188.
[4] S. Jing, L. Zhang, L. Luo, J. Lu ,S. Yun ,P.K. Shen, P. Tsiakaras , N-Doped Porous Molybdenum Carbide Nanobelts as Efficient Catalysts for Hydrogen Evolution Reaction, Appl. Catal. 224 (2018) 533-540.
[5] R. Kothari, D. Buddhi, R.L. Sawhney, Comparison of environmental and economic aspects of various hydrogen production methods, Renew. Sustain. Energy Rev. 12 (2008) 553–563.
[6] A. Flamos, P.G. Georgallis, H. Doukas, J. Psarras, Using biomass to achieve European Union energy targets-a review of biomass status, potential, and supporting policies, Int. J. Green Energy 8 (2011) 411–428 .
[7] E. Gürtekin, Biological Hydrogen Production Methods, 2Nd Int. Symp. Environ. Moral. C (2014) 463–471.
[8] S. Liu, J. Zhu, M. Chen, W. Xin, Z. Yang, L. Kong, Hydrogen production via catalytic pyrolysis of biomass in a two-stage fixed bed reactor system, Int. J. Hydrogen Energy 39(25) (2014) 13128–13135.
[9] M. Farrag, Ultrasmall bimetallic Ru-Co alloy nanoclusters immobilized in amino-functionalized UiO-66 and N-doped carbonaceous zirconium oxide nanocomposite for hydrogen generation, J. Alloys Compd. 920 (2022) 165893.
[10] M. Farrag, G.A.M. Ali, Hydrogen generation of single alloy Pd/Pt quantum dots over Co3O4 nanoparticles via the hydrolysis of sodium borohydride at room temperature, Sci. Rep. 12 (2022) 17040.
[11] H.N. Abdelhamid, Z. Huang, A.M. El-Zohry, H. Zheng, X. Zou, A Fast and Scalable Approach for Synthesis of Hierarchical Porous Zeolitic Imidazolate Frameworks and One-Pot Encapsulation of Target Molecules, Inorg. Chem. 56(15) (2017) 9139–9146.
[12] Y. Yang, K. Chen , J.Z. Lin, Y. Zhou ,Q.Y. Liu, C. Hang , H.N. Abdelhamid, Z.Q. Zhang, H. Chen ,A Zn-MOF constructed from electron-rich π-conjugated ligands with an interpenetrated graphene-like net as an efficient nitroaromatic sensor, RSC Adv. 6 (2016) 45475–45481.
[13] H.N. Abdelhamid , X. Zou, Template-free and room temperature synthesis of hierarchical porous zeolitic imidazolate framework nanoparticles and their dye and CO2 sorption, Green Chem. 20 (2018) 1074–1084.
[14] A.F. Abdel-Magied, H.N. Abdelhamid, R.M. Ashour, X. Zou, K. Forsberg, Hierarchical porous zeolitic imidazolate frameworks nanoparticles for efficient adsorption of rare-earth elements, Microporous Mesoporous Mater. 278 (2019) 175–184.
[15] Z. Chen, S. L. Hanna, L. R. Redfern, D. Alezi, T. Islamoglu, and O. K. Farha, Reticular chemistry in the rational synthesis of functional zirconium cluster-based MOFs, Coord. Chem. Rev. 386 (2019) 32–49.
[16] H.N. Abdelhamid, Surfactant assisted synthesis of hierarchical porous metal-organic frameworks nanosheets, Nanotechnol. 30 (2019) 435601.
[17] Z. Lu, L. Guo, Q. Shen, F. Bi, C. Li, X. Zhang, The application of metal–organic frameworks and their derivatives in the catalytic oxidation of typical gaseous pollutants: Recent progress and perspective, Sep. Purif. Technol. 340 (2024) 126772.
[18] R. Rao, S. Ma, B. Gao, F. Bi, Yifan Chen, Y. Yang, N. Liu, M. Wu, X. Zhang, Recent advances of metal-organic framework-based and derivative materials in the heterogeneous catalytic removal of volatile organic compounds, J. Colloid Interface Sci. 636 (2023) 55-72.

[19] S. Gulati, S. Vijayan, Mansi, S. Kumar, B. Harikumar, M. Trivedi, R.S. Varma, Recent advances in the application of metal-organic frameworks (MOFs)-based nanocatalysts for direct conversion of carbon dioxide (CO2) to value-added chemicals, Coord. Chem. Rev. 474 (2023) 214853.
[20] S.F. Hammad, I.A. Abdallah, A.Bedair, R.M. Abdelhameed, M. Locatelli, F.R. Mansour, Metal organic framework-derived carbon nanomaterials and MOF hybrids for chemical sensing, TrAC 170 (2024) 117425.
[21] U. Hou, L. Wang, Y. Gao, J. Ping, F. Zhao, Recent advances in metal-organic framework-based nanozymes and their enabled optical biosensors for food safety analysis, TrAC 173 (2024) 117602.
[22] M. Ahmadian, H. Derakhshankhah, M. Jaymand, Recent advances in adsorption of environmental pollutants using metal–organic frameworks-based hydrogels, Int. J. Biol. Macromol. 231 (2023) 123333.
[23] S. Naghdi, M.M. Shahrestani, M. Zendehbad, H. Djahaniani, H. Kazemian, D. Eder, Recent advances in application of metal-organic frameworks (MOFs) as adsorbent and catalyst in removal of persistent organic pollutants (POPs), J. Hazard. Mater. 442 (2023) 130127.
[24] B. Chen, Z. Yang, Q. Jia, R. J. Ball, Y. Zhu, Y. Xia, Emerging applications of metal-organic frameworks and derivatives in solar cells: Recent advances and challenges, Mater. Sci. Eng. R: Rep. 152 (2023) 100714.
[25] N. Muzaffar, A.M. Afzal, H.H. Hegazy, M.W. Iqbal, Recent advances in two-dimensional metal-organic frameworks as an exotic candidate for the evaluation of redox-active sites in energy storage devices, J. Energy Storage 64 (2023) 107142.
[26] W. Zou, L. Zhang, J. Lu, D. Sun, Recent development of metal–organic frameworks in wound healing: Current status and applications, J. Chem. Eng. 480 (2024) 148220.
[27] N. Rabiee, Sustainable metal-organic frameworks (MOFs) for drug delivery systems, Mater. Today Commun. 35 (2023) 106244.
[28] U. Munawar, M.S. Khan, S.E.Z. Syeda, S. Nawaz, F.A. Janjhi, H. Haq, E.U. Rashid, T. Jesionowski, M. Bilal, Metal-organic framework-based smart nanoplatforms for biosensing, drug delivery, and cancer theranostics, Inorg. Chem. Commun. 147 (2023) 110145.
[29] H. Liu, J. Zhang, D. Ao, Construction of heterostructured ZnIn2S4@NH2-MIL-125(Ti) nanocomposites for visible-light-driven H2 production, Appl. Catal. 221 (2018) 433–442.
[30] A. Abraham, R. Silviya, R. Patel, N. Patel, R. Fernandes, MOF derived cobalt-phospho-boride for rapid hydrogen generation via NaBH4 hydrolysis, Int. J. Hydrogen Energy 77 (2024) 1245-1253.
[31] H. Gao, C. Ding, J. Wang, G. Ding, Y. Xue, Y. Zhang, K. Zhang, P. Liu, X. Gao, Cobalt nanoparticles packaged into nitrogen-doped porous carbon derived from metal-organic framework nanocrystals for hydrogen production by hydrolysis of sodium borohydride, Int. J. Hydrogen Energy 44(16) (2019) 8365-8375.
[32] A.A. Kassem, H.N. Abdelhamid, D.M. Fouad, S.A. Ibrahim, Metal-organic frameworks (MOFs) and MOFs-derived CuO@C for hydrogen generation from sodium borohydride, Int. J. Hydrogen Energy 44(59) (2019) 31230-31238.
[33] K-Y. A. Lin, H-A. Chang, Efficient hydrogen production from NaBH4 hydrolysis catalyzed by a magnetic cobalt/carbon composite derived from a zeolitic imidazolate framework, J. Chem. Eng. 296 (2016) 243-251.
[34] D.D. Tuan, K.-Y. A. Lin, Ruthenium supported on ZIF-67 as an enhanced catalyst for hydrogen generation from hydrolysis of sodium borohydride, J. Chem. Eng. 351 (2018) 48-55.
[35] J.M.F. Morales, L.A. Lozano, E.C. López , I.R. Ramos, A.G. Ruiz, and J.M. Zamaro, Direct sulfation of a Zr-based metal-organic framework to attain strong acid catalysts, Microporous Mesoporous Mater. 290 (2019) 1387-1811.
[36] H.N. Abdelhamid, Solid Acid Zirconium Oxo Sulfate/Carbon-Derived UiO-66 for Hydrogen Production, Energy & Fuels 35(12) (2021) 10322-10326.
[37] M. Saikia , L. Saikia, Sulfonic acid-functionalized MIL-101(Cr) as a highly efficient heterogeneous catalyst for one-pot synthesis of 2-amino-4H-chromenes in aqueous medium, RSC Adv. 6 (2016) 15846-15853.
[38] Z. Zhao , M. Liu, K. Zhou, H. Gong, Y. Shen, Z. Bao, Q. Yang, Q. Ren, Z. Zhang, Zr-Based Metal–Organic Frameworks with Phosphoric Acids for the Photo-Oxidation of Sulfides, Int. J. Mol. Sci. 23(24) (2022) 16121.
[39] D.P. Phan ,E.Y. Lee, Phosphoric acid enhancement in a Pt-encapsulated Metal-Organic Framework (MOF) bifunctional catalyst for efficient hydro-deoxygenation of oleic acid from biomass, J. Catal. 386 (2020) 19–29
[40] C. Wang, A.R. Li, Y.L. Ma, Phosphomolybdic acid niched in the metal-organic framework UiO-66 with defects: An efficient and stable catalyst for oxidative desulfurization, Fuel Process. Technol. 212 (2021) 106629.
[41] X. Zhang, Z. Zhang, B. Zhang, X. Yang, X. Chang, Z. Zhou, D.H. Zhang, X.H. Bu, Synergistic effect of Zr-MOF on phosphomolybdic acid promotes efficient oxidative desulfurization, Appl. Catal. 256 (2019) 117804.
[42] P. Verma, R. V. Singh, A. M. Banerjee, M. R. Pai, Enhanced photocatalytic hydrogen generation using UiO-66(Zr) MOF with tailored modifications: A review, Int. J. Hydrogen Energy (2024) .
[43] Y. Wang, L. Gudiño, J. Bedia, C. Belver, Solar photocatalytic hydrogen production through metal sulfide/UiO-66-NH2 heterojunctions, Sep. Purif. Technol. 353(C) (2025) 128663.
[44] Y. Bi, X.Wang, K. Li, C. Wang, Y. Zhang, Q. Liu, Ni_2P derived from Ni-MOF supported on UiO-66-NH_2 to boost CdS photocatalytic hydrogen production, COLLOID SURF. A-PHYSICOCHEM. ENG. ASP. 702(1) (2024) 134929.
[45] C.-Y. Hsu, W.-T. Chung, T-M. Lin, R.-X. Yang, S. S. Chen, K. C.-W. Wu, Coking-resistant NiO@CeO2 catalysts derived from Ce-MOF for enhanced hydrogen production from plastics, Int. J. Hydrogen Energy 49(D) (2024) 873-883.
[46] H.N. Abdelhamid, UiO-66 as a catalyst for hydrogen production: Via the hydrolysis of sodium borohydride, Dalt. Trans. 49 (2020) 10851–10857.
[47] J.M. Yassin, A.M. Taddesse, M.S. Sanchez, Room temperature synthesis of high-quality Ce (IV) -based MOFs in water, Microporous Mesoporous Mater. 324 (2021) 111303.

[48] F.T. Alshorifi, D.E. Tobbala, S.M. El-Bahy, M.A. Nassan, and R.S. Salama, The role of phosphotungstic acid in enhancing the catalytic performance of UiO-66 (Zr) and its applications as an efficient solid acid catalyst for coumarins and dihydropyrimidinones synthesis, Catal. Commun. 169 (2022) 106479.
[49] W. Sun, X. Li, C. Sun, Z. Huang, H. Xu, W. Shen, Insights into the pyrolysis processes of Ce-MOFs for preparing highly active catalysts of toluene combustion, Catalysts, 9(8) (2019) 682.
[50] X. Liao, X. Wang, F. Wang, Y. Yao, S. Lu, Ligand Modified Metal Organic Framework UiO-66: A Highly Efficient and Stable Catalyst for Oxidative Desulfurization, J Inorg. Organomet. Polym. Mater. 31 (2021) 756–762.
[51] F. Khosravi, M. Gholinejad, J.M. Sansano, R. Luque, Bimetallic Fe–Cu metal organic frameworks for room temperature catalysis, Appl. Organomet. Chem. 36 (2022) 6749.
[52] S. Subudhi, G. Swain, S.P. Tripathy, K. Parida, UiO-66-NH2Metal-Organic Frameworks with Embedded MoS2Nanoflakes for Visible-Light-Mediated H2 and O2 Evolution, Inorg. Chem. 59(14) (2020) 9824–9837.
[53] A. Raghi, K. Ghani, M. Jafari, Modification of UiO-66 for removal of uranyl ion from aqueous solution by immobilization of tributyl phosphate, J. Chem. Sci. 133 (2021) 14.
[54] A.S. Elsherbiny, A. Rady, R.M. Abdelhameed, A.H. Gemeay, Efficiency and selectivity of cost-effective Zn-MOF for dye removal, kinetic and thermodynamic approach, Environ. Sci. Pollut. Res. 30 (2023) 106860–106875.
[55] N. Riezzati, Y.K. Krisnandi, A. Zulys, Metal organic frameworks of lanthanum and iron using BDC linker as catalysts for glucose conversion into 5-hydroxymethylfurfural (5-HMF), IOP Conf. Ser.: Mater. Sci. Eng. 902 (2020) 012044.
[56] X. Zhang, Z. Zhang, B. Zhang, X. Yang, X. Chang, Z. Zhou, D.H. Wang, M.H. Zhang, X.H. Bu, Synergistic effect of Zr-MOF on phosphomolybdic acid promotes efficient oxidative desulfurization, Molecules 256 (2020) 4673.
[57] A. Nikseresht, R. Bagherinia, M. Mohammadi, R. Mehravar, Phosphomolybdic acid hydrate encapsulated in MIL-53 (Fe): a novel heterogeneous heteropoly acid catalyst for ultrasound-assisted regioselective nitration of phenols, RSC Adv. 13 (2022) 674–687.
[58] A.A. Ibrahim, M.M. Kaid, S.L. Ali, S.E. Samra, S.A. El-Hakam, A.I. Ahmed, Applications of nanostructure phosphomolybdic acid/strontium MOF for removal of Rhodamine B and synthesis of pharmaceutically significant 14-Aryl-14-alkyl-14-H-dibenzoxanthene and 7-hydroxy-4-methyl coumarin, Inorg. Chem. Commun. 153 (2023) 110748.
[59] J. D. Wang, D. Li, J. K. Liu, X. H. Yang, J. L. He, Y. Lu, One-Step Preparation and Characterization of Zinc Phosphate Nanocrystals with Modified Surface, Soft Nanoscience Letters. 1 (2011) 81–85.
[60] N. Vollmer, R. Ayers, Decomposition combustion synthesis of calcium phosphate powders for bone tissue engineering, Int. J. Self-Propagating High-Temp. Synth. 21 (2012) 189–201.
[61] M. Amine, F. Asafar, L. Bilali, M. Nadifiyine, Hydrochloric Acid Leaching Study of Rare Earth Elements from Moroccan Phosphate, J Chem. 2019 (2019).
[62] M. Hallquist, D.J. Stewart, S.K. Stephenson, R.A. Cox, Hydrolysis of N2O5 on sub-micron sulfate aerosols, PCCP 5 (2003) 3453–3463.
[63] A. Kumar, S. Dubey, Utilization of natural gypsum for the preparation of ammonium sulfate, Chem. Pap. 77 (2023) 2707–2716.
[64] G. Das, N. Kakati, S.H. Lee, N. Karak, Y.S. Yoon, Water soluble sodium sulfate nanorods as a versatile template for the designing of copper sulfide nanotubes, J. Nanosci. Nanotechnol. 14(6) (2014) 4455–4461.
[65] T. Wang, L. Han, X. Li, T. Chen, S. Wang, Functionalized UiO-66-NH2 by trimellitic acid for highly selective adsorption of basic blue 3 from aqueous solutions, Front Chem. 10 (2022) 962383.
[66] K.V. Savunthari, C.H. Yi, J.Y. Huang, K. Iputera, S.F. Hu, R.S. Liu, All-Solid-State Na-O2Batteries with Long Cycle Performance, ACS Appl. Energy Mater. 5(11) (2022) 14280–14289.
[67] H. Li, M. Fu, S.Q. Wang , X. Zhang , M. Zhao, F. Yang , C.Y. Tang, Y. Dong, Stable Zr-Based Metal-Organic Framework Nanoporous Membrane for Efficient Desalination of Hypersaline Water, Environ. Sci. Technol. 55(21) (2021) 14917–14927.
[68] S. Wang, M. Ma ,W. Man, Q. Zhang, X. Niu , G. Sun , W. Zhang , T. Jiao , One-step facile fabrication of sea urchin-like zirconium oxide for efficient phosphate sequestration, RSC Adv. 5 (2015) 91218–91224.
[69] H. Li, H. Chu, X. Ma, G. Wang, F. Liu, M. Guo, W. Lu, S. Zhou, M. Yu, Efficient heterogeneous acid synthesis and stability enhancement of UiO-66 impregnated with ammonium sulfate for biodiesel production, J. Chem. Eng. 408 (2021) 127277.
[70] X. Fang, S. Wu, Y. Wu, W. Yang, Y. Li , J. He, P. Hang, M. Nie, C. Xie , Z. Wu, K. Zhang, L. Kong, J. Liu, High-efficiency adsorption of norfloxacin using octahedral UIO-66-NH2 nanomaterials: Dynamics, thermodynamics, and mechanisms, Appl. Surf. Sci. 518 (2020) 15979.
[71] S. Ravi , S. Zhang , Y.R. Lee, K.K. Kang, J.W. Ahn, W.S. Ahn ,EDTA-functionalized KCC-1 and KIT-6 mesoporous silicas for Nd3+ ion recovery from aqueous solutions, J. Ind. Eng. Chem. 67 (2018) 210–218.
[72] H.J. Kim, J.N. Heo, J.Y. Do, S.J. Yoon, Y. Kim, M. Kang, Hydrogen production improvement on water decomposition through internal interfacial charge transfer in M3(PO4)2-M2P2O7 mixed-phase catalyst (M = Co, Ni, and Cu), Catalysts 9(7) (2019) 602.
[73] Y. Chen, Z. Lu, M. Qian, H. Zhang, C. Chen, H. Xie , F.R. Tay, Chemical affinity of 10-methacryloyloxydecyl dihydrogen phosphate to dental zirconia: Effects of molecular structure and solvents, Dent. Mater. J. 33(12) (2017) 415–427.
[74] T. Chhabra, J. Rohilla, V. Krishnan, Nanoarchitectonics of phosphomolybdic acid supported on activated charcoal for selective conversion of furfuryl alcohol and levulinic acid to alkyl levulinates, Mol. Catal. 519 (2022) 112135.
[75] A. Kaur, D. Gangacharyulu, and P.K. Bajpai, Kinetic studies of hydrolysis reaction of NaBH4 with γ-Al2O3 nanoparticles as catalyst promoter and CoCl2 as catalyst, Braz. J. Chem. Eng. 36(2) (2019) 929–939.
[76] J. Andrieux, U.B. Demirci, J. Hannauer, C. Gervais, C. Goutaudier, P. Miele, Spontaneous hydrolysis of sodium borohydride in harsh conditions, Int. J. Hydrogen Energy 36(1) (2011) 224–233.

[77] R. Retnamma, A.Q. Novais, C.M. Rangel, Kinetics of hydrolysis of sodium borohydride for hydrogen production in fuel cell applications: A review, Int. J. Hydrogen Energy 36(16) (2011) 9772–9790.
[78] C.M. Kaufman, B. Sen, Hydrogen Generation by Hydrolysis of Sodium Tetrahydroborate : Effects of Acids and Transition Metals and their Salts, J. Chem. Soc., Dalton Trans. (1985) 307-313.
[79] B.K.A. Holbrook, P.G. Twist , Hydrolysis of the Borohydrides Ion catalyzed by Metal-Boron Alloys, J. Chem. Soc. A (1971) 890-894.
[80] M. Mitov, R. Rashkov, N. Atanassov, A. Zielonka, Effects of nickel foam dimensions on catalytic activity of supported Co-Mn-B nanocomposites for hydrogen generation from stabilized borohydride solutions, J. Mater. Sci. 42 (2007) 3367–3372.
[81] H.B. Dai, Y. Liang, P. Wang, X.D. Yao, T. Rufford, M. Lu, H.M. Cheng, High-performance cobalt-tungsten-boron catalyst supported on Ni foam for hydrogen generation from alkaline sodium borohydride solution, Int. J. Hydrogen Energy, 33 (2008) 4405–4412.
[82] D. Hua, Y. Hanxi, A. Xinping, C. Chuansin, Hydrogen production from catalytic hydrolysis of sodium borohydride solution using nickel boride catalyst, 28 (2003) 1095-1100.
[83] S.U. Jeong, R.K. Kim, E.A. Cho, H.J. Kim, S.W. Nam, I.H. Oh, S.A. Hong. , S.H. Kim, A study on hydrogen generation from NaBH4 solution using the high-performance Co-B catalyst, J. Power Sources 144 (2005) 129–134.
[84] B.H. Liu, Z.P. Li, S. Suda, Nickel- and cobalt-based catalysts for hydrogen generation by hydrolysis of borohydride, J. Alloys Compd. 415 (2006) 288–293. .
[85] S.C. Amendola, S.L. Sharp-Goldman, M. Saleem-Janjua, M.T. Kelly, P.J. Petillo, M. Binder, An ultrasafe hydrogen generator: aqueous, alkaline borohydride solutions and Ru catalyst, J. Power Sources 85 (2000) 186-189.
[86] J. Zhao, H. Ma, J. Chen, Improved hydrogen generation from alkaline NaBH4 solution using carbon-supported Co - B as catalysts, Int. J. Hydrogen Energy 32 (2007) 4711–4716.
[87] J.C. Ingersoll, N. Mani, J.C. Thenmozhiyal, A. Muthaiah, Catalytic hydrolysis of sodium borohydride by a novel nickel-cobalt-boride catalyst, J. Power Sources, 173 (2007) 450–457.
[88] C. L. Hsueh, C.Y. Chen, J.R. Ku, Y.Y. Hsu, S.F. Tsai, M.S. Jeng, Simple and fast fabrication of polymer template-Ru composite as a catalyst for hydrogen generation from alkaline NaBH4 solution, J. Power Sources 177 (2008) 485–492.
[89] H. Bin-Dai, Y. Liang, P. Wang, H. M. Cheng, Amorphous cobalt-boron/nickel foam as an effective catalyst for hydrogen generation from alkaline sodium borohydride solution, J. Power Sources 177 (2008) 17–23. .
[90]W. Ye, H. Zhang, D. Xu, L. Ma, B. Yi, Hydrogen generation utilizing alkaline sodium borohydride solution and supported cobalt catalyst, J. Power Sources 164 (2007) 544–548.
[91] L. Valenzano, B. Civalleri, S.M. Chavan, S. Bordiga ,M.H. Nilsen, S.Jacokobsen, K.P. Lilleruel , C. Lamberti, Disclosing the complex structure of UiO-66 metal organic framework: A synergic combination of experiment and theory, Chem. Mater. 23 (2011) 1700–1718..
[92] J. Hajek, B. Bueken, M. Waroquier, D. De Vos, V. Van Speybroeck, The Remarkable Amphoteric Nature of Defective UiO-66 in Catalytic Reactions, Chem. Cat. Chem. 9 (2017) 2203–2210.
[93] C.D. Fast, J. Woods, J. Lentchner, T.A. Makal, Stabilizing defects in metal-organic frameworks: Pendant Lewis basic sites as capping agents in UiO-66-type MOFs toward highly stable and defective porous materials, Dalton Trans. 48 (2019) 14696–14704.
[94] C. Saka, Oxygen and nitrogen-doped metal-free microalgae carbon nanoparticles for efficient hydrogen production from sodium borohydride in methanol, Int. J. Hydrogen Energy 46 (2021) 26298–26307.
[95] C.C. Su, M.C. Lu, S.L. Wang, Y.H. Huang, Ruthenium immobilized on Al2O3 pellets as a catalyst for hydrogen generation from hydrolysis and methanolysis of sodium borohydride, RSC Adv. 2 (2012) 2073–2079.
[96] J.H. Kim, K.T. Kim, Y.M. Kang, H. S. Kim, M.S. Song, Y.U. Lee , P.S. Lee, J.Y. Lee Study on degradation of filamentary Ni catalyst on hydrolysis of sodium borohydride, J. Alloys Compd. 379(1-2) (2004) 222–227.
[97] D. Xu, P. Dai, X. Liu, C. Cao, Q. Guo, Carbon-supported cobalt catalyst for hydrogen generation from alkaline sodium borohydride solution, J. Power Sources 182(2) (2008) 616–620.
[98] K. Narasimharao, B.M. Abu-Zied, S.Y. Alfaifi, Cobalt oxide supported multi wall carbon nanotube catalysts for hydrogen production via sodium borohydride hydrolysis, Int. J. Hydrogen Energy 46(9) (2021) 6404–6418.